

Optimization of 7-T Chemical Exchange Saturation Transfer Parameters for Validation of Glycosaminoglycan and Amide Proton Transfer of Fibroglandular Breast Tissue¹

Adrienne N. Dula, PhD
Blake E. Dewey, BS
Lori R. Arlinghaus, PhD
Jason M. Williams, PhD
Dennis Klomp, PhD
Thomas E. Yankeelov, PhD
Seth Smith, PhD

Purpose:

To (a) implement simulation-optimized chemical exchange saturation transfer (CEST) measurements sensitive to amide proton transfer (APT) and glycosaminoglycan (GAG) hydroxyl proton transfer effects in the human breast at 7 T and (b) determine the reliability of these techniques for evaluation of fibroglandular tissue in the healthy breast as a benchmark for future studies of pathologic findings.

Materials and Methods:

All human studies were institutional review board approved, were HIPAA compliant, and included informed consent. The CEST parameters of saturation duration (25 msec) and amplitude (1 μ T) were chosen on the basis of simulation-driven optimization for APT contrast enhancement with the CEST effect quantified by using residuals of a Lorentzian fit. Optimized parameters were implemented at 7 T in 10 healthy women in two separate examinations to evaluate the reliability of CEST magnetic resonance (MR) imaging measurements in the breast. CEST z-spectra were acquired over saturation offset frequencies ranging between ± 40 ppm by using a quadrature unilateral breast coil. The imaging-repeat imaging reliability was assessed in terms of the intraclass correlation coefficient, which indicates the ratio of between-subject variation to total variation.

Results:

Simulations were performed of the Bloch equations with chemical exchange-guided selection of optimal values for pulse duration and amplitude, 25 msec and 1 μ T, respectively. Reliability was evaluated by using intraclass correlation coefficients (95% confidence intervals), with acceptable results: 0.963 (95% confidence interval: 0.852, 0.991) and 0.903 (95% confidence interval: 0.609, 0.976) for APT and GAG, respectively.

Conclusion:

Simulations were used to derive optimal CEST preparation parameters to elicit maximal CEST contrast enhancement in healthy fibroglandular breast tissue due to APT at 7 T. By using these parameters, reproducible values were obtained for both the amide and hydroxyl protons from CEST MR imaging at 7 T and are feasible in the human breast.

© RSNA, 2014

¹From the Institute of Imaging Science (A.N.D., B.E.D., L.R.A., J.M.W., D.K., T.E.Y., S.S.), Department of Radiology and Radiological Sciences (A.N.D., T.E.Y., S.S.), Program in Chemical and Physical Biology (T.E.Y., S.S.), Department of Biomedical Engineering (T.E.Y., S.S.), Department of Physics and Astronomy (T.E.Y., S.S.), Department of Cancer Biology (T.E.Y.), and Vanderbilt Ingram Cancer Center (T.E.Y.), Vanderbilt University Medical Center, AA-1105 Medical Center North, 1161 21st Ave S, Nashville, TN 37232-2310; and Department of Radiology, University Medical Center Utrecht, Utrecht, the Netherlands. Received April 11, 2014; revision requested May 14; final revision received August 11; final version accepted September 6. **Address correspondence to A.N.D.** (e-mail: adrienne.n.dula@vanderbilt.edu).

As tumors undergo a myriad of chemical changes, the metabolic by-products may be indirectly measured with chemical exchange saturation transfer (CEST) magnetic resonance (MR) imaging using endogenous metabolite sensitivity enhancement through exchange with water protons (1). The sensitivity of CEST to these subtle chemical changes may provide complementary biomarkers of pathologic findings to conventional (T1- and T2-weighted) MR imaging while providing fundamentally different information than that provided with established quantitative techniques.

CEST MR imaging uses the transfer of saturation to study mobile compounds within tissue by selectively saturating labile protons such as those residing in amide bonds of proteins or peptides (amide proton transfer [APT]) and hydroxyl moieties using narrow-bandwidth radiofrequency irradiation. This saturation is transferred to bulk water, causing the water signal to be slightly attenuated. The resulting water signal is observed as a function of saturation frequency relative to water, termed the z-spectrum (2), because the water pool is much larger than the saturated solute proton pool, and each exchanging saturated solute proton is replaced by a nonsaturated

water proton, which is then again saturated. This activity results in signal enhancement and allows the presence of low-concentration solutes to be examined indirectly. CEST has been used to examine cancer in the brain (3) and the breast (4–6), leading to detection of increased APT in tumor because of differences in pH and protein content inside cells. This sensitivity to intracellular protein content provides valuable information in regard to the viability and health of fibroglandular (FG) tissue. The increased APT signal found in tumors has been attributed to an increase in free protein concentration in malignant cells (3,7,8). While APT has been studied in a myriad of oncology applications, hydroxyl exchange represents a largely unexplored area, particularly in the breast, where glycosaminoglycan (GAG) content could be an important indicator of tissue status. As active mediators in cell-cell and cell-matrix interactions, proteoglycans significantly affect neoplastic cell behavior (9) with increased proteoglycan content found in mammary tumors (10).

While access to APT moieties can be obtained at lower field strengths, the hydroxyl protons of GAG are less accessible due to their rapid exchange rate and proximity to the water resonance. There have been no prior studies of CEST targeted at hydroxyl protons performed at lower field strengths, such as 1.5 T or 3.0 T (11,12). These previously inaccessible protons can be studied at 7 T because of increased chemical dispersion, facilitating selective saturation, decreasing pulse bandwidth demands, and a favorable exchange regimen. In addition, higher field strength translates to higher achievable spatial resolution, better anatomic coverage, or a decreased imaging time. Our goal was to optimize CEST acquisition and analysis to minimize and characterize variability in CEST-derived APT and hydroxyl proton transfer (derived from GAG) measurements in healthy FG breast tissue at 7 T.

Materials and Methods

All human studies were institutional review board approved, Health Insurance Portability and Accountability

Act compliant and included informed consent. Data were obtained by using a whole-body 7-T MR imaging system (Achieva; Philips Medical Systems, Cleveland, Ohio).



Simulations

Theoretical saturation was modeled according to the Bloch equations (13). This modeling was performed with transfer effects modified for steady-state and time-dependent magnetization for CEST (14) to optimize preparation (radiofrequency irradiation power and bandwidth) for chemical exchange occurring at approximately 3.5 ppm (APT CEST) and 1.5 ppm (GAG CEST) downfield from water in healthy breast

Advances in Knowledge

- This study provides optimal parameters and establishes reliability of 7-T chemical exchange saturation transfer (CEST) MR imaging of the breast with intraclass correlation coefficients of 0.963 (95% confidence interval: 0.852, 0.991) and 0.903 (95% confidence interval: 0.609, 0.976) for amide proton transfer and glycosaminoglycan, respectively.
- This study describes frequency drift correction for isolation of CEST effects.
- This study establishes the clinically important level of change for application of CEST MR imaging in breast pathologic findings.

Published online before print

10.1148/radiol.14140762 Content codes:  

Radiology 2015; 275:255–261

Abbreviations:

APT = amide proton transfer
 APT_{LoF} = integrated area between the Lorentzian fit and z-spectrum expressed as CEST_{LoF} for APT
 CEST = chemical exchange saturation transfer
 CEST_{LoF} = integrated area between the Lorentzian fit and z-spectrum
 FG = fibroglandular
 GAG = glycosaminoglycan
 GAG_{LoF} = integrated area between the Lorentzian fit and z-spectrum for GAG
 ICC = intraclass correlation coefficient
 k_{ex} = exchange rate
 S = observed signal intensity
 S₀ = observed signal intensity with saturation far off resonance (80 ppm)

Author contributions:

Guarantor of integrity of entire study, A.N.D.; study concepts/study design or data acquisition or data analysis/interpretation, all authors; manuscript drafting or manuscript revision for important intellectual content, all authors; approval of final version of submitted manuscript, all authors; agrees to ensure any questions related to the work are appropriately resolved, all authors; literature research, A.N.D., B.E.D., L.R.A., J.M.W., D.K., T.E.Y.; clinical studies, A.N.D., L.R.A., S.S.; experimental studies, A.N.D., B.E.D., D.K., T.E.Y., S.S.; statistical analysis, A.N.D., B.E.D., T.E.Y., S.S.; and manuscript editing, A.N.D., L.R.A., J.M.W., D.K., T.E.Y., S.S.

Funding:

This research was supported by the National Institutes of Health (grants NCI 1R01CA129961, NCI 1P50 098131, NIH P30 CA68485, NCI 1U01CA142565, NCI 1U01CA174706, NIBIB K01EB009210, and KL2 RR24977).

Conflicts of interest are listed at the end of this article.

tissue at 7 T, with use of software (Matlab 2012b; Mathworks, Natick, Mass). The magnetization profile at a frequency offset from water, defined by $\Delta\omega$, was studied by using the matrix solution (14) in a three-pool model (15) including (a) a labile, slow exchange resonance (CEST) centered at $\Delta\omega$ of 3.5 ppm and 1.5 ppm for APT and GAG, respectively; (b) a direct water saturation component at $\Delta\omega$ of 0 ppm; and (c) an asymmetric magnetization transfer component centered at $\Delta\omega$ of -2.34 ppm. We examined the effects of varying saturation parameters on APT and hydroxyl resonances, which were calculated by integrating the CEST effect between 3.0–4.0 ppm and 1.0–2.0 ppm, respectively.

The saturation pulse power (B_1 amplitude) was modeled as a 30-msec single-lobed sinc-Gauss pulse from 1 μ T to 3 μ T. Next, B_1 amplitude was fixed to 1 μ T, while pulse duration was varied from 0 to 60 msec. A three-dimensional pulsed-CEST approach (16) was chosen by using a single radiofrequency irradiation every repetition time, creating a cumulative saturation effect and building up steady state over multiple short repetition times. Physical constants included the following: (a) water protons, where T1 was 2.3 seconds, and T2 was 45 msec; (b) amide protons, where T1 was 1.0 seconds, T2 was 20 msec, and the exchange rate (k_{ex}) was 50 sec^{-1} ; (c) hydroxyl protons, where T1 was 1.0 seconds, T2 was 40 msec, and k_{ex} was 500 sec^{-1} ; and (d) magnetization transfer, where T1 was 1.6 seconds, T2 was 0.001 msec, and k_{ex} was 20 sec^{-1} (5,17).

Subjects

Ten women (median age, 24 years; age range, 22–33 years) with no history of breast disease underwent two MR imaging examinations occurring within 2 weeks of each other (median, 4 days; range, 1–14 days).

MR Imaging

A local transmit-receive breast coil (MR Coils BV, Drunen, the Netherlands) (18) was used for unilateral radiofrequency transmission and reception.

CEST data were acquired by using a three-dimensional gradient-echo, multishot sequence (six shots). Fat suppression included a water-selective binomial excitation pulse train with an interpulse separation of 0.5 msec to allow a short echo time of 2.7 msec. The dynamic image time was 10.2 seconds, and repetition time was 20.0 msec. The acquisition matrix was $152 \times 152 \times 12$ over a $150 \text{ mm} \times 150 \text{ mm} \times 72 \text{ mm}$ field of view. The nominal excitation was 3.6° , the estimated Ernst angle for glandular tissue at 7 T that was based on the previously published T1 (17) and prescribed repetition time.

Saturation was achieved by using a 25-msec, 1- μ T sinc-Gauss pulse applied at 44 saturation-offset frequencies ($\Delta\omega$) between ± 40 ppm with saturation far off resonance ($\Delta\omega = 80$ ppm) acquired twice at the beginning of the sequence, once at the end, and interleaved every five acquisitions, resulting in a total of 56 images. The proximity of the breast to the lungs creates a time-dependent B_0 field fluctuation, which can be deconvolved from the overall CEST effect by calculating time-varying observed signal intensity (S) with saturation far off resonance (80 ppm) (S_0), as discussed in Data Analysis below (19).

Data Analysis

Image coregistration used a nonrigid three-dimensional affine transformation (20). The healthy FG tissue was isolated by using semiautomated segmentation, as previously described (4). The signal intensities as a function of saturation offset frequency ($S[\Delta\omega]$) from images acquired with saturation far off resonance were defined as $S_0 = S(\Delta\omega = 80 \text{ ppm})$. The S_0 images were fit to a cubic spline as a function of time to calculate the z-spectrum as $S(\Delta\omega)/S_0$ based on acquisition time. To correct for field inhomogeneities, points of the z-spectrum selected to exclude the resonances of interest for APT and GAG ($\Delta\omega$ between 1 and 5 ppm) were fit to a single Lorentzian function, and the minima was assigned to the water frequency ($\Delta\omega = 0$ ppm). The CEST effect was calculated as the integrated area between the Lorentzian

fit and z-spectrum, termed $CEST_{Lor}$ for amide proton transfer (APT_{Lor}) associated with proteins and peptides (21), where $\Delta\omega$ is between 3.0 and 4.0 ppm and hydroxyl protons associated with GAG (integrated area between the Lorentzian fit and z-spectrum for GAG [GAG_{Lor}], termed GAG_{CEST}) where $\Delta\omega$ is between 1.0 and 2.0 ppm (22).

Statistical Analysis

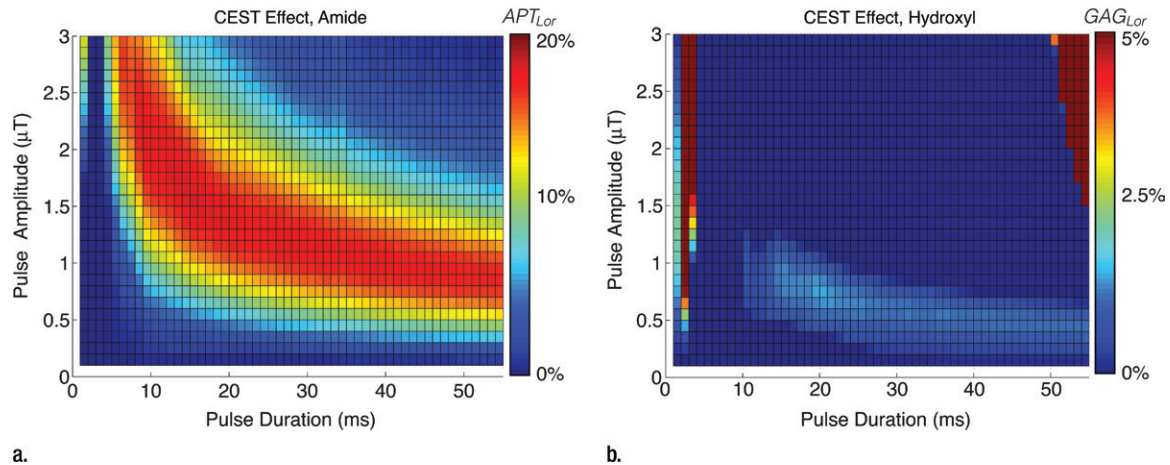
Statistical analysis was performed by using software (SPSS R19; IBM, Armonk, NY). Imaging-repeat imaging CEST-derived indexes for APT_{Lor} and GAG_{Lor} were compared in two ways. Bland-Altman analysis was used to determine variability between mean values of the two examinations for each subject ($n = 10$) (23), with the mean difference evaluated in comparison with the limits of agreement. More important, if the 95% confidence interval for the mean difference includes zero, this supports the null hypothesis that there is no imaging-repeat imaging difference ($\alpha = .05$). The imaging-repeat imaging reliability was assessed in terms of the intraclass correlation coefficient (ICC) (24) according to the following equation: $R = V_{bs}/V_{bs} + E$, where R is reliability, V_{bs} is between-subject variability, and E is error. The ICC-derived reliability indicates the ratio of between-subject variation to total variation (ie, it is the sum of within- and between-subject variation using mean squared values derived from within-subject repeated-measures analysis of variance. With this procedure, we can establish the threshold for a measured difference to be biophysical rather than measurement noise.

Results

Simulation Data

Simulation results for both APT_{Lor} and GAG_{Lor} are displayed in Figure 1a and 1b, respectively. $CEST_{Lor}$ is shown as a function of pulse duration and amplitude, with maximum APT_{Lor} contrast enhancement found for pulse amplitudes of 0.5–1.5 μ T within the pulse duration range of 15–40 msec. More important, this range of saturation

Figure 1

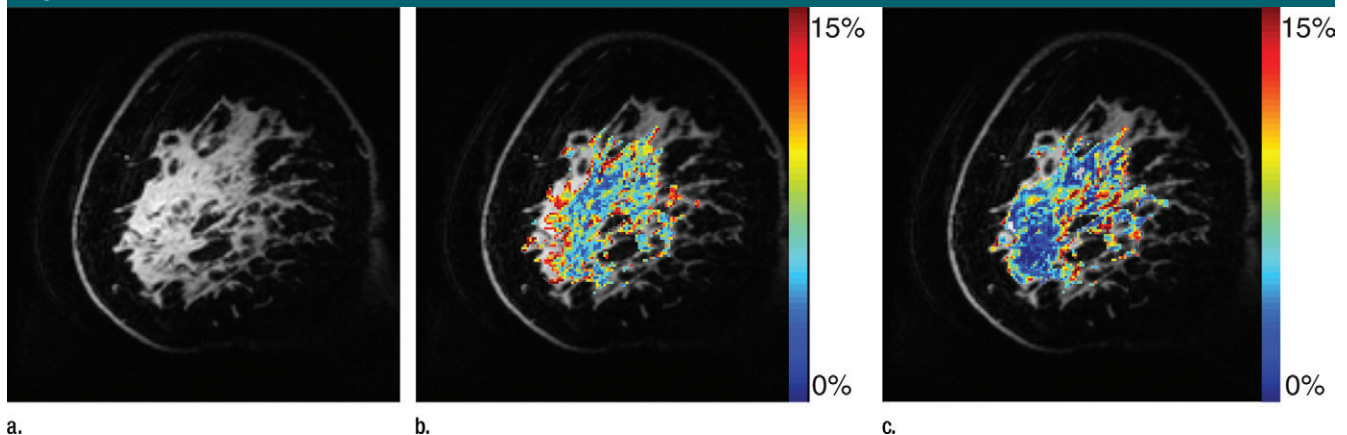


a.

b.

Figure 1: Simulation of pulsed CEST MR imaging guiding saturation parameters. **(a)** APT CEST effect and **(b)** GAG CEST effect as a function of saturation pulse amplitude and duration. Choosing saturation parameters eliciting optimal APT and minimum image time, hydroxyl proton exchange simulations indicate potential to detect this fast-exchanging moiety, as well. *ms* = Milliseconds.

Figure 2



a.

b.

c.

Figure 2: Example images from CEST MR imaging data set. **(a)** S_0 image acquired with a saturation offset of 80 ppm provides anatomic detail. **(b)** APT_{Lor} map calculated by using an image acquired following saturation at 3.5 ppm downfield from water depicts an increased amide exchange affect in anterior glandular tissue. **(c)** GAG_{Lor} map calculated by using an image acquired 1.6 ppm downfield from water that is associated with hydroxyl protons. Color bar = percentage of signal intensity change.

amplitudes and durations corresponds to a maximum for both APT_{Lor} and GAG_{Lor} and, therefore, saturation pulse parameters were chosen as 25-msec duration with 1.0- μ T amplitude to capture both resonances.

MR Imaging Data

Example test-repeat test data are shown in Figure 2; Figure 2a presents an S_0 image, with $\Delta\omega = 80$ ppm; Figure 2b presents the APT_{Lor} map calculated

at $\Delta\omega$ between 3 and 4 ppm; and Figure 2c presents the GAG_{Lor} map calculated at $\Delta\omega$ between 1 and 2 ppm. The time variation of S_0 data is seen in Figure 3a, with S_0 signal intensity of masked FG tissue shown as a function of acquisition time (black dots) with the calculated spline fit (black line). Example z-spectra calculated by using the uncorrected mean value of 12 S_0 images (gray line) and detrended z-spectra (black line) are shown in Figure 3b.

The noncorrected data show large deviations around the APT resonance and signal intensity variations caused by nuclear Overhauser enhancement (25), observed in previous studies of GAG CEST (22). Detrending minimizes influence from upfield resonances, but CEST effects around 3.5 and 1.5 ppm (APT and GAG, respectively) remain. Cohortwise CEST results are shown in Figure 4. Figure 4a depicts the mean z-spectra derived from masked FG

Figure 3

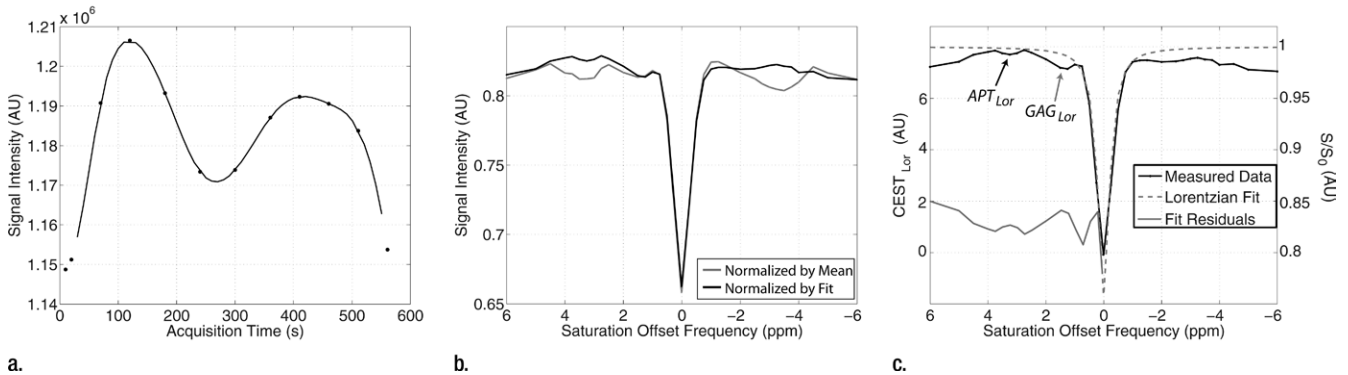


Figure 3: Details of CEST MR imaging data acquisition and processing. **(a)** Mean signal intensity of masked FG tissue in S_0 image volumes (black dots) acquired intermittently used for z-spectrum normalization, where $\Delta\omega = 80$ ppm, plotted as a function of acquisition time. A cubic spline fit (black line) was used to extrapolate S_0 signal intensities. **(b)** Example z-spectra normalized by the mean of the S_0 signal intensities (gray line) and that normalized by the extrapolated S_0 values from the spline fit (black line). **(c)** Example z-spectra (black line, right y-axis) with Lorentzian fit (dashed gray line, right y-axis) used to calculate the APT_{Lor} (black arrow) and GAG_{Lor} (gray arrow) from the residuals of the fit (gray line, left y-axis). AU = arbitrary units, s = seconds.

Figure 4

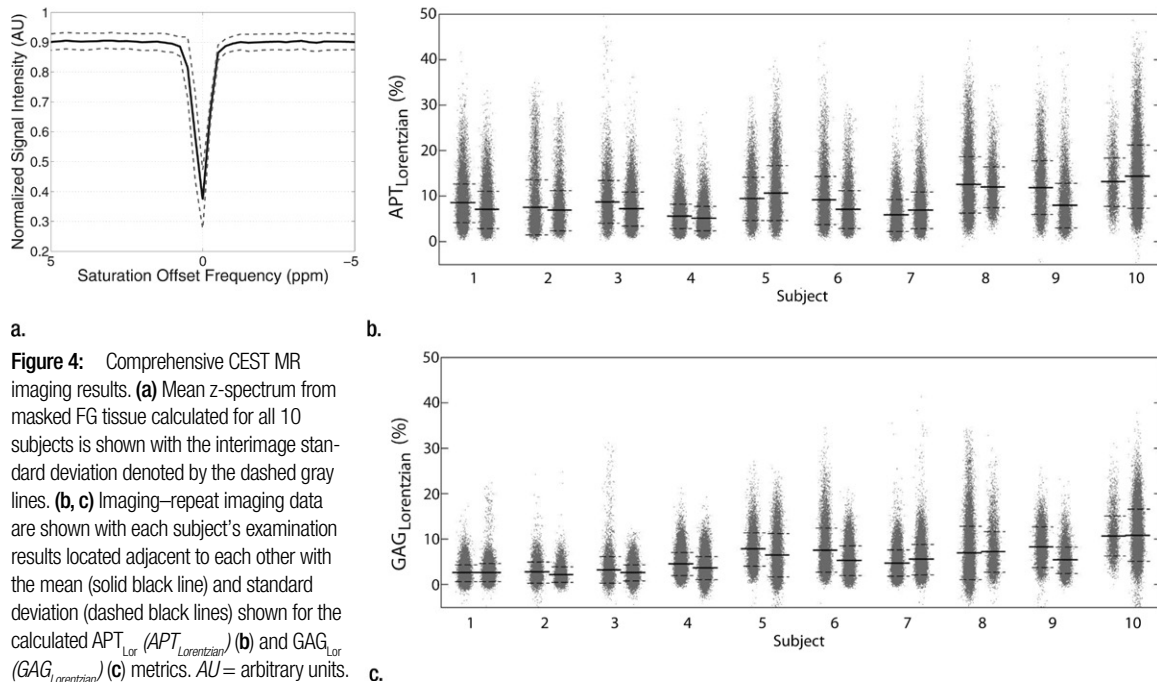


Figure 4: Comprehensive CEST MR imaging results. **(a)** Mean z-spectrum from masked FG tissue calculated for all 10 subjects is shown with the interimage standard deviation denoted by the dashed gray lines. **(b, c)** Imaging-repeat imaging data are shown with each subject's examination results located adjacent to each other with the mean (solid black line) and standard deviation (dashed black lines) shown for the calculated APT_{Lor} ($APT_{Lorentzian}$) **(b)** and GAG_{Lor} ($GAG_{Lorentzian}$) **(c)** metrics. AU = arbitrary units.

tissue of all data (solid black line) ($n = 10$ subjects, two examinations each), and the interimage standard deviation is represented by dashed gray lines. These results can be examined on a voxel-by-voxel basis where calculated APT_{Lor} (Fig 4b) and GAG_{Lor} (Fig 4c) for each of the 10 healthy subjects' images

are shown side by side for comparison of the means (solid black line) and the standard deviations (dashed gray line). Figure 4a demonstrates overall intersubject repeatability, while Figure 4b and 4c indicates that the mean and standard deviation were comparable for each subject's repeated measures.

Statistical Analysis Data

Bland-Altman plots are shown in Figure 5 with subjectwise differences plotted against the mean value for each subjects' APT_{Lor} (Fig 5a) and GAG_{Lor} (Fig 5b) measurements. By using the calculated standard error of the mean (0.45% for APT_{Lor} and 0.17% for

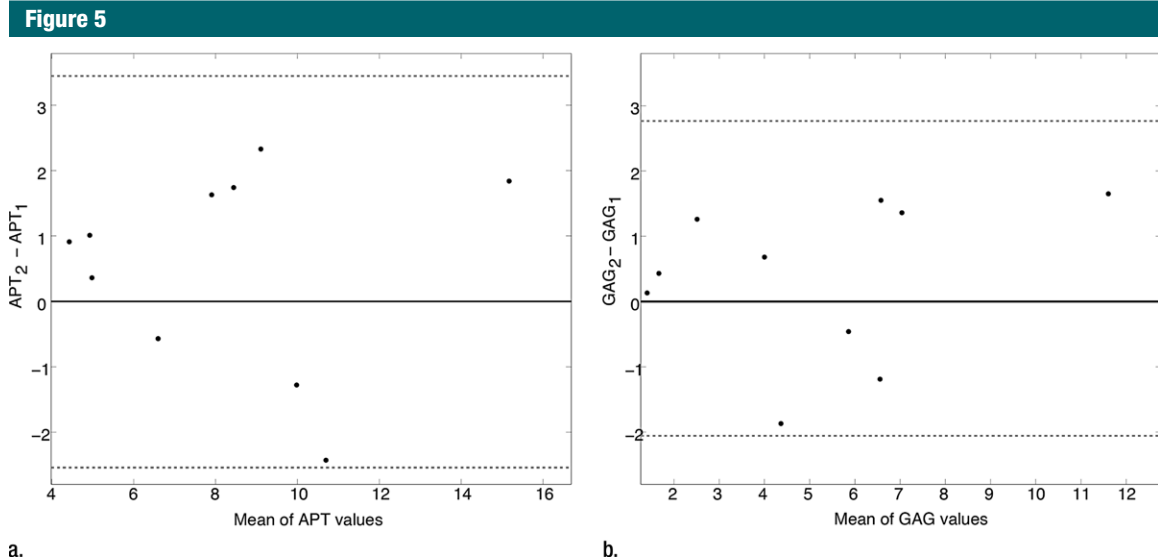


Figure 5: Test–repeat test results for masked FG of 10 healthy subjects. Bland–Altman plots for **(a)** APT_{Lor} and **(b)** GAG_{Lor} show the difference between the mean image values for each subject (black dots) plotted against the mean of the respective CEST-derived metric. The mean difference values (solid black lines) and limits of agreement (dotted gray lines) are shown for both metrics.

GAG_{Lor}), mean differences were 0.41% for APT_{Lor} and 0.61% for GAG_{Lor} (indicated by the solid black lines), neither of which were significantly different from zero. The limits of agreement were -2.54% to 3.45% for APT_{Lor} and -2.06% to 2.77% for GAG_{Lor} ($\alpha = .05$) and are indicated by the dotted gray lines in Figure 5. Using the equation, the reliability of mean values was 2.93 and 2.53 for APT_{Lor} and GAG_{Lor}, respectively. The resulting ICC for average measures of APT_{Lor} was 0.963 (95% confidence interval: 0.852, 0.991), and it was 0.903 (95% confidence interval: 0.609, 0.976) for GAG_{Lor}.

Discussion

This study presents optimization of acquisition parameters, a processing technique to simultaneously study the CEST effect for two resonances (APT and GAG) of interest in the breast, and evaluation of reliability in healthy FG tissue in vivo at 7 T. The method for quantification of the CEST effect can have a large effect on calculated indexes, particularly reproducibility. The imaging–repeat imaging reliability values (2.93 for APT_{Lor} and 2.35 for GAG_{Lor}) can be interpreted as the

noise-to-signal ratio (ie, the inverse of the APT_{Lor} signal-to-noise ratio); however, this metric is also sensitive to both systematic and random variation between the imaging–repeat imaging events (26). We extended test–repeat test analyses to include the ICC, with the resulting ICC values for both APT and GAG CEST being greater than 0.90, indicating strong agreement between examinations, as well as their potential value in future clinical studies.

Given the sample size ($n = 10$) of this initial study, it is difficult to control for age and menstrual cycle effects, which are known to modulate breast tissue density and composition (27). Further studies will include in-traitage registration to account for such effects. In addition, the ICC is a composite measure precluding isolation of specific sources of variability. Finally, future simulations will explore attainable contrast-to-noise ratio for expected pathologic changes in CEST effects.

The current standard of care for MR imaging examination of breast disease involves 1.5-T evaluation of morphometric changes and contrast agent distribution on the basis of MR

images, providing nonspecific assessment of tumor characteristics. We leveraged increased field strength to provide reliable quantitative metabolic information noninvasively with the potential to detect tissue abnormalities by establishing the clinically relevant difference for detection of pathologic findings. Through evaluation of variability in healthy glandular tissue, it is possible to define a change in measured CEST effect that is clinically substantial, which is important for future diagnostic and prognostic studies. Thus, the potential for high-field-strength CEST MR imaging in the breast is substantial and is important, as the capability to assess resonances that may play a key role in understanding breast disease cannot be captured by alternative techniques or lower magnetic field strengths.

Acknowledgment: We acknowledge Hakmook Kang, PhD (Department of Biostatistics, Vanderbilt University School of Medicine, Nashville, Tenn) for biostatistical input.

Disclosures of Conflicts of Interest: A.N.D. disclosed no relevant relationships. B.E.D. disclosed no relevant relationships. L.R.A. disclosed no relevant relationships. J.M.W. disclosed no relevant relationships. D.K. disclosed no relevant relationships. T.E.Y. Activities re-

lated to the present article: disclosed no relevant relationships. Activities not related to the present article: received personal fees from Eli Lilly & Co. Other relationships: disclosed no relevant relationships. **S.S.** disclosed no relevant relationships.

References

- Goffeney N, Bulte JW, Duyn J, Bryant LH Jr, van Zijl PC. Sensitive NMR detection of cationic-polymer-based gene delivery systems using saturation transfer via proton exchange. *J Am Chem Soc* 2001;123(35):8628–8629.
- Ward KM, Aletras AH, Balaban RS. A new class of contrast agents for MRI based on proton chemical exchange dependent saturation transfer (CEST). *J Magn Reson* 2000;143(1):79–87.
- Jones CK, Schlosser MJ, van Zijl PC, Pomper MG, Golay X, Zhou J. Amide proton transfer imaging of human brain tumors at 3T. *Magn Reson Med* 2006;56(3):585–592.
- Dula AN, Arlinghaus LR, Dortch RD, et al. Amide proton transfer imaging of the breast at 3 T: establishing reproducibility and possible feasibility assessing chemotherapy response. *Magn Reson Med* 2013;70(1):216–224.
- Schmitt B, Zamecnik P, Zaiss M, et al. A new contrast in MR mammography by means of chemical exchange saturation transfer (CEST) imaging at 3 Tesla: preliminary results. *Rofo* 2011;183(11):1030–1036.
- Klomp DW, Dula AN, Arlinghaus LR, et al. Amide proton transfer imaging of the human breast at 7T: development and reproducibility. *NMR Biomed* 2013;26(10):1271–1277.
- Zhou J, Blakeley JO, Hua J, et al. Practical data acquisition method for human brain tumor amide proton transfer (APT) imaging. *Magn Reson Med* 2008;60(4):842–849.
- Zhou J, Lal B, Wilson DA, Laterra J, van Zijl PC. Amide proton transfer (APT) contrast for imaging of brain tumors. *Magn Reson Med* 2003;50(6):1120–1126.
- Iozzo RV. Proteoglycans and neoplasia. *Cancer Metastasis Rev* 1988;7(1):39–50.
- Alini M, Losa GA. Partial characterization of proteoglycans isolated from neoplastic and nonneoplastic human breast tissues. *Cancer Res* 1991;51(5):1443–1447.
- Haris M, Cai K, Singh A, Hariharan H, Reddy R. In vivo mapping of brain myo-inositol. *Neuroimage* 2011;54(3):2079–2085.
- van Zijl PC, Jones CK, Ren J, Malloy CR, Sherry AD. MRI detection of glycogen in vivo by using chemical exchange saturation transfer imaging (glycoCEST). *Proc Natl Acad Sci U S A* 2007;104(11):4359–4364.
- Woessner DE. Nuclear transfer effects in nuclear magnetic resonance pulse experiments. *J Chem Phys* 1961;35(1):41–48.
- Woessner DE, Zhang S, Merritt ME, Sherry AD. Numerical solution of the Bloch equations provides insights into the optimum design of PARACEST agents for MRI. *Magn Reson Med* 2005;53(4):790–799.
- Desmond KL, Stanisz GJ. Understanding quantitative pulsed CEST in the presence of MT. *Magn Reson Med* 2012;67(4):979–990.
- Jones CK, Polders D, Hua J, et al. In vivo three-dimensional whole-brain pulsed steady-state chemical exchange saturation transfer at 7 T. *Magn Reson Med* 2012;67(6):1579–1589.
- Haddadin IS, McIntosh A, Meisamy S, et al. Metabolite quantification and high-field MRS in breast cancer. *NMR Biomed* 2009;22(1):65–76.
- Klomp DW, van de Bank BL, Raaijmakers A, et al. 31P MRSI and 1H MRS at 7 T: initial results in human breast cancer. *NMR Biomed* 2011;24(10):1337–1342.
- Jones CK, Huang A, Xu J, et al. Nuclear Overhauser enhancement (NOE) imaging in the human brain at 7T. *Neuroimage* 2013;77:114–124.
- Netsch T, van Muiswinkel A. Quantitative evaluation of image-based distortion correction in diffusion tensor imaging. *IEEE Trans Med Imaging* 2004;23(7):789–798.
- Zhou J, Payen JF, Wilson DA, Traystman RJ, van Zijl PC. Using the amide proton signals of intracellular proteins and peptides to detect pH effects in MRI. *Nat Med* 2003;9(8):1085–1090.
- Ling W, Regatte RR, Navon G, Jerschow A. Assessment of glycosaminoglycan concentration in vivo by chemical exchange-dependent saturation transfer (gagCEST). *Proc Natl Acad Sci U S A* 2008;105(7):2266–2270.
- Bland JM, Altman DG. Statistical methods for assessing agreement between two methods of clinical measurement. *Lancet* 1986;1(8476):307–310.
- Koch G. Intraclass correlation coefficient. In: Kotz S, Johnson NL, eds. *Encyclopedia of statistical sciences*. New York, NY: Wiley, 1982; 213–217.
- van Zijl PC, Zhou J, Mori N, Payen JF, Wilson D, Mori S. Mechanism of magnetization transfer during on-resonance water saturation: a new approach to detect mobile proteins, peptides, and lipids. *Magn Reson Med* 2003;49(3):440–449.
- Landman BA, Bazin PL, Smith SA, Prince JL. Robust estimation of spatially variable noise fields. *Magn Reson Med* 2009;62(2):500–509.
- de Lima CR, de Arimatéa dos Santos Junior J, Nazário AC, Michelacci YM. Changes in glycosaminoglycans and proteoglycans of normal breast and fibroadenoma during the menstrual cycle. *Biochim Biophys Acta* 2012;1820(7):1009–1019.